

Quantum image classifier with single photons

Kunkun Wang,¹ Lei Xiao,¹ Wei Yi,^{2,3,*} Shi-Ju Ran,^{4,†} and Peng Xue^{1,‡}

¹Beijing Computational Science Research Center, Beijing 100084, China

²CAS Key Laboratory of Quantum Information, University of Science and Technology of China, Hefei 230026, China

³CAS Center For Excellence in Quantum Information and Quantum Physics, Hefei 230026, China

⁴Department of Physics, Capital Normal University, Beijing 100048, China

Machine learning, with promising applications in quantum computation, has been introduced to a variety of quantum mechanical platforms, where its interplay with quantum physics offers exciting prospects toward quantum advantages. A central difficulty, however, lies in the access and control of the large Hilbert space required by quantum machine learning protocols, through the limited number of noisy qubits available to near-term quantum devices. Whereas it is recognized that a viable solution lies in the design of quantum algorithms that incorporates quantum entanglement and interference, a demonstration of quantum machine learning protocols capable of solving practical tasks is still lacking. Here we report the classification of real-life, hand-drawn images on a quantum mechanical platform of single photons. Adopting a tensor-network-based machine learning algorithm with an entanglement-guided optimization, we achieve an efficient representation of the quantum feature space using matrix product states. This allows us to demonstrate image classification with a high success rate using single-photon interferometry networks. Our experiment establishes a general and scalable framework for quantum machine learning, which is readily accessible on other physical platforms.

Introduction:—The interdisciplinary field of quantum machine learning has seen astonishing progresses recently [1, 2], where novel algorithms presage useful applications for near-term quantum computers, and offer a feasible route toward quantum advantages. A concrete example is pattern recognition, where modeling in the exponentially large quantum Hilbert space, typical in quantum classifiers, can lead to unique advantages over their classical counterparts [3–5]. Such a quantum advantage originates from the efficient exploitation of quantum entanglement, which also underlies the extraordinary interpretability of tensor networks (TNs), a powerful theoretical framework that originates from quantum information science and has found wide applications in the study of strongly-correlated many-body systems [6–9]. Recent works have revealed that TN-based machine learning algorithms, due to their quantum nature, exhibit competitive, if not better, performance compared to classical machine learning models such as supportive vector machines [3, 10–13] and neural networks [14–24]. It is thus tempting to demonstrate TN-based machine learning algorithms on genuine quantum platforms, with the hope of tackling practical tasks. However, major obstacles exist, as TN-based machine learning algorithms typically require an unwieldily large Hilbert space to process real-life data. The problem is made worse by the limited number of noisy qubits in the currently available quantum platforms. So far, TN-based machine learning has yet to be demonstrated on any physical system.

In this work, we experimentally demonstrate the classification of hand-drawn images on a quantum mechani-

cal platform of single photons, using TN-based machine learning algorithms. As a key element of our scheme, we combine the interpretability of TN with an entanglement-based optimization, such that the dimension of the required Hilbert space is dramatically reduced [25]. We are then able to implement the corresponding quantum circuits through single-photon interferometry. Focusing on the minimal task of classifying hand-written digits of “0” and “1” [26], we demonstrate two TN-based machine learning schemes, each with three- and five-layer constructions corresponding to an increasing dimension of the quantum feature space. The gate operations in the single-photon interferometry network are optimized through supervised learning on classical computers, and results of the classification are read out through projective measurements on the output photons. Based on our experimental results, we estimate an over 98% success rate with both of our schemes for classifying the hand-written digits. While our hybrid quantum-classical optimization scheme can be further upgraded to be fully quantum mechanical, the TN-based machine learning algorithm demonstrated here is quite general and scalable. In light of the recent progress of machine learning either on quantum platforms [3, 13, 27–32], or with classical-quantum hybrid setups [33–39], our experiment paves the way for quantum advantages in solving real-world problems.

Supervised machine learning by discriminative TNs:—As illustrated in Fig. 1, we implement TN-based quantum classifier through the following steps: (i) map the data of classical images to product states in the Hilbert space (quantum feature space); (ii) project the product state onto the TN-based classifier in the form of an orthogonal TN state, which is subsequently encoded into a qubit-efficient scheme that directly corresponds to implementable quantum circuits; (iii) optimize parameters

* wyiz@ustc.edu.cn

† sjran@cnu.edu.cn

‡ gnepx@gmail.com

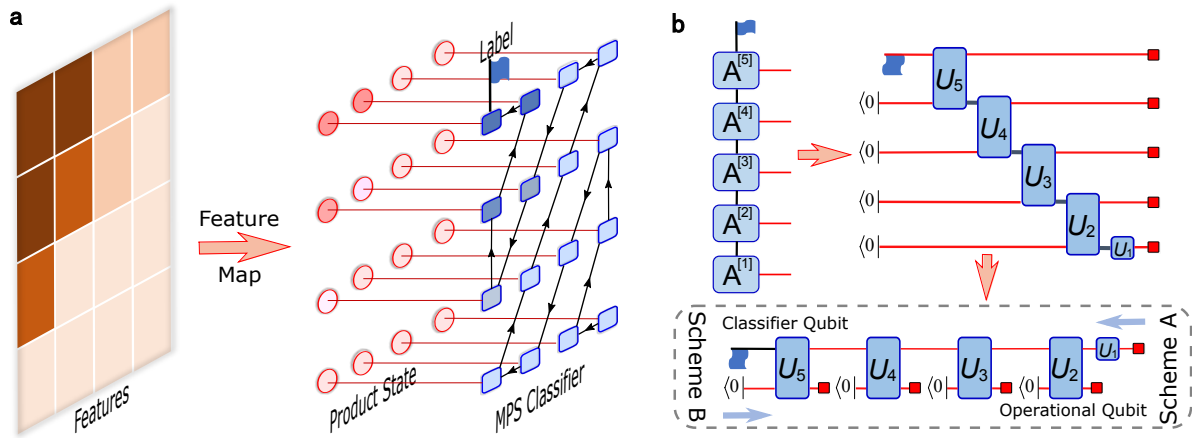


FIG. 1. **Illustration of the TN-based quantum classifier.** **a** Features of a classical image, such as pixels or frequency components, are mapped to a product state in the quantum feature space (Hilbert space), which is subsequently projected onto the TN-based classifier (right-most layer) consisting of the label index, represented by a flag, and tensors of the matrix product state (MPS), represented by squares. The MPS is kept in an orthogonal form, indicated by arrows on the virtual bonds. We re-arrange the features, such that the more important ones (darker color), characterized by larger entanglements with the rest of the quantum feature space, are closer to the label index. **b** Retaining only a handful of features with large entanglement in the MPS classifier, we encode the classifier state, represented by tensors $A^{[i]}$ [$i = 1, \dots, 5$; see Eq. (4)], into the qubit-efficient scheme [35] (within the dashed box), which directly corresponds to quantum circuits of the two schemes implemented in our experiment. Here we use a five-layer construction as an example, which involves two qubits, a single-qubit gate U_1 , and four two-qubit gates U_i ($i = 2, \dots, 5$). We define the two qubits as the classifier qubit (upper) and the operational qubit (lower). The red dots represent projection (scheme A) or projective measurements (scheme B) in the basis of the retained features, and $|0\rangle$ corresponds to projection (scheme B) or projective measurements (scheme A) in the basis state $|0\rangle$ of the operational qubit.

of the quantum circuit through supervised learning with a set of labeled images; (iv) feed quantum features of the images to be classified into the quantum circuit and perform projective measurements on the output state, where the classification results correspond to the category with the largest probability. Whereas the training process in (iii) is performed on a classical computer, we achieve an efficient representation of the classical image in the Hilbert space in steps (i) and (iv), facilitated by both the interpretability of TNs and the entanglement-based optimization.

More concretely, for a classical gray-scale image consisting of N features (pixels or frequency components), we follow the general recipe of TN-based supervised learning [17, 18] and map the classical image to a product state of N qubits in the quantum Hilbert space

$$|\phi\rangle = \prod_{\otimes n=1}^N |s_n\rangle, \quad (1)$$

with the feature map given by

$$|s_n\rangle = \cos \frac{x_n \pi}{2} |0\rangle + \sin \frac{x_n \pi}{2} |1\rangle. \quad (2)$$

Here $0 \leq x_n \leq 1$ characterizes the n th feature and determines the superposition coefficients of the n th qubit $|s_n\rangle$ in the basis $\{|0\rangle, |1\rangle\}$.

To classify a set of images into N_c categories, we introduce a quantum classifier state $|\Psi\rangle$ in a joint Hilbert space $\mathcal{H}_{|\phi\rangle} \otimes \mathcal{H}_c$, where $\mathcal{H}_{|\phi\rangle}$ denotes the Hilbert space of

the product state in Eq. (2) and \mathcal{H}_c is the N_c -dimensional Hilbert space encoding the information of different categories. The classifier state should be constructed in such a way that, for any given unclassified image with the mapped quantum state $|\phi\rangle$, the probability of this image belonging to the c th category is

$$P_c = |\langle \Psi | (|\phi\rangle \otimes |c\rangle)|^2, \quad (3)$$

where $\{|c\rangle\}$ is the orthonormal basis in \mathcal{H}_c representing the N_c categories. Hence, P_c constitutes the probability distribution for different categories of a given classical image, which, as we demonstrate later, can be probed via projective measurements according to Eq. (3). The prediction of the classifier is given by the category with the largest probability (i.e., $\text{argmax}_c P_c$).

While the core of the supervised quantum machine learning is the construction of $|\Psi\rangle$ with minimal overall error in classifying images of the training set, the challenge is how to efficiently represent and optimize $|\Psi\rangle$. Such a goal is particularly demanding for real-life images with a typical number of pixels $N \sim O(10^2)$ or larger, since the dimension of the many-body entangled state $|\Psi\rangle$ scales exponentially with N . To address the issue, we use TNs to represent the classifier state, and reduce the dimensionality of the Hilbert space by exploiting its entanglement properties.

Following the common practice in the TN-based machine learning, we use matrix product state (MPS) [6,

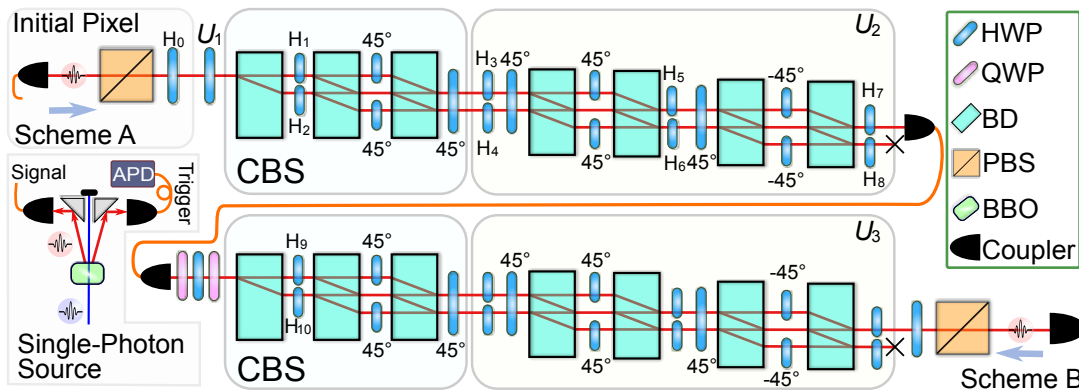


FIG. 2. **Experimental demonstration of quantum classifier with the three-layer construction.** For each pair of photons generated by spontaneous parametric down conversion, one photon serves as the trigger and the other, the signal photon, proceeds through the experimental setup corresponding to the two schemes. Under Scheme A, the signal photon is projected onto the polarization state $|\psi_1\rangle$ of the classifier qubit via a polarizing beam splitter (PBS) and a half-wave plate (HWP) H_0 . It is then sent through an interferometric network, composed of HWPs and beam displacers (BDs), before detected by avalanche photodiodes (APDs) in coincidence with the trigger photon. The single-qubit gate U_1 is realized by a HWP, and two-qubit gates U_2 and U_3 are realized by BDs and HWPs. The input states $|\psi_2\rangle$ and $|\psi_3\rangle$ are encoded in the spatial modes of photons, and are prepared via the HWPs (H_1 , H_2 , H_9 , and H_{10}) in controlled beam splitters (CBSs) which, by combining the spatial and polarization degrees of freedom, effectively expand the dimension of the system. A 1m long single-mode fiber serves as a spatial filter in between successive modules of two-qubit gate, and a set of wave plates is introduced to offset the impact of the fiber on the photon polarizations. For detection, photons are projected onto upper spatial mode $|u\rangle$ by discarding those in the lower one, and a projective measurement of σ_z is realized through a HWP, a PBS and APDs. Scheme B is the exact reverse process of Scheme A, where photons are sent into the setup through the output port of Scheme A (see Supplemental Materials).

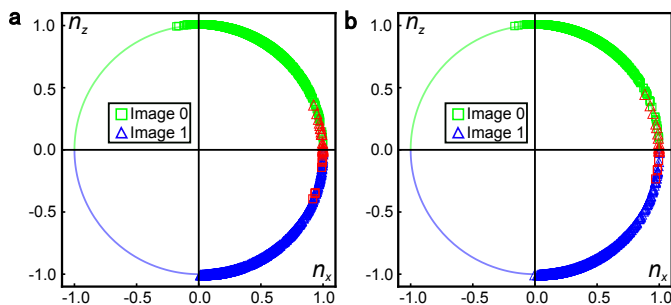


FIG. 3. **Theoretical results of the testing set.** Results obtained under **a** the three-layer construction and **b** the five-layer construction, respectively. The output states are shown in the x - z plane of Bloch sphere associated with the classifier qubit. The green squares (blue triangles) indicate successful recognition of the hand-written digit “0” (“1”). Red symbols indicate cases in which the classifier fails to recognize the image.

17, 40] to represent $|\Psi\rangle$ as

$$|\Psi\rangle = \sum_{\{s\}} \sum_{\{a\}} \sum_c A_{s_N, c a_{N-1}}^{[N]} \cdots A_{s_2, a_2 a_1}^{[2]} A_{s_1, a_1}^{[1]} \prod_{n=1}^N |s_n\rangle |c\rangle. \quad (4)$$

For the subscripts of tensors $A^{[i]}$ ($i = 1, \dots, N$), $\{s_n\}$ are the physical indices labeling the feature qubits in the Hilbert space, $\{a_n\}$ are the virtual indices to be con-

tracted in the simulation, and the label index c that is unique to $A^{[N]}$ lives in \mathcal{H}_c and represents the categories. For our purpose, we take the dimension of the label index $\dim(c) = N_c = 2$ for the binary classification. We also take the dimension of the virtual index $\dim(a_n) = 2$ ($n = 1, \dots, N - 1$), so that the classification can be implemented with only qubits.

To train the MPS, meaning to optimize the tensors in Eq. (4), we define the loss function as the negative-log likelihood

$$f = - \sum_{m \in \mathcal{I}} \ln P_{c^{(m)}}, \quad (5)$$

where \mathcal{I} denotes the training set, $P_{c^{(m)}}$ is defined by Eq. (3) and $c^{(m)}$ denotes the correct category of the m th image. The training process thus involves the minimization of f from the training set, which is equivalent to the maximization of the accuracy of classifying the training samples [41]. To this end, we apply the environment method [18], in which tensors are kept as isometries. This allows us to encode the MPS into a quantum circuit that is executable on quantum platforms [35, 42]. Specifically, the gate operations in the quantum circuit are directly determined by the tensors $A^{[i]}$ (see Methods for details).

To run the TN-based machine learning on our photonic platform, we reduce the required number of qubits by adopting an entanglement-based optimization method of the MPS architecture [25]. In essence, in the product state Eq. (4), we only retain a handful of core feature qubits which possess the largest entanglement with other

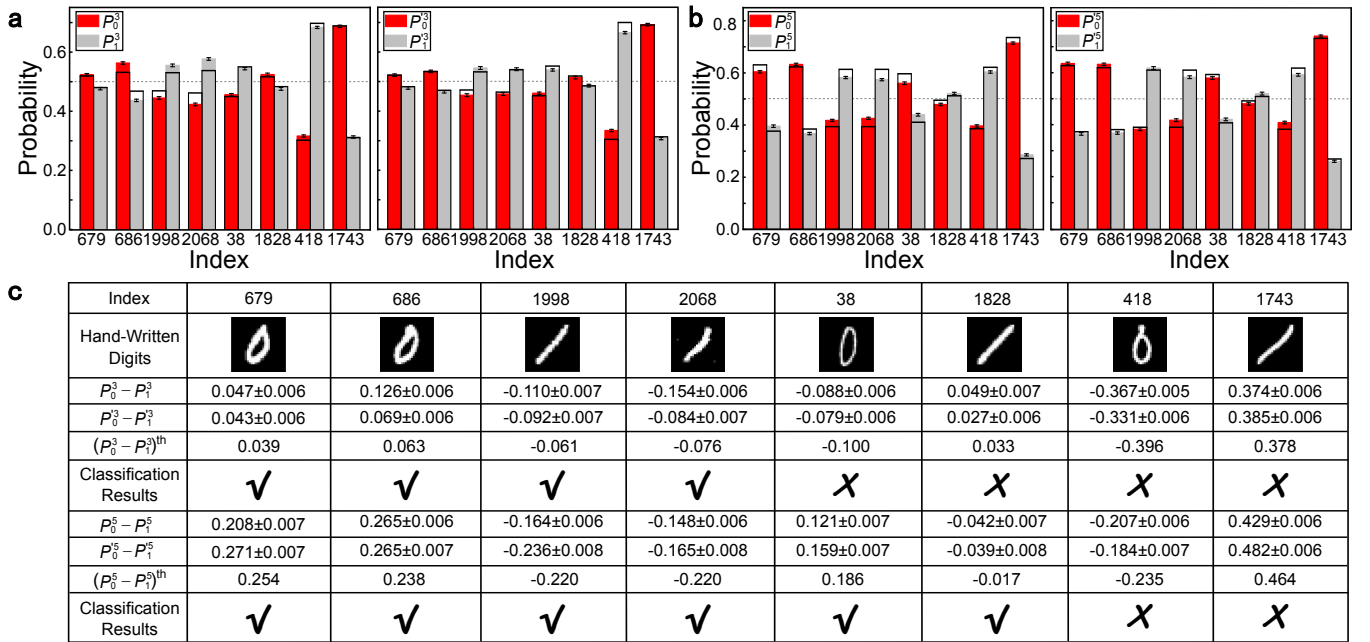


FIG. 4. **Experimental classification of images within the testing set.** Measured probabilities of the projective measurements on output states of quantum classifiers with the three- **a** and five-layer **b** constructions. Left: Scheme A; right: Scheme B. Colored bars represent experimental results, while hollow bars represent their theoretical predictions. Error bars indicate the statistical uncertainty, obtained by assuming Poissonian statistics in the photon-number fluctuations. **c** The classification results for eight typical hand-written digits in the testing set. Rows represent the index of images, the hand-written digits, the experimental and theoretical probability differences, and classification results. $P_{0,1}^3$ and $P_{0,1}^5$ represent probabilities associated with the three- and five-layer constructions, respectively.

qubits in the classifier state $|\Psi\rangle$. We denote the states of these extracted feature qubits as $\{|\psi_i\rangle\}$, and re-arrange them such that features with larger entanglements are closer to the label index c in $A^{[N]}$. Under a similar construction as Eq. (1), the product state for an image becomes $\prod_{\otimes i} |\psi_i\rangle$ after the feature-extraction procedure. The number of tensors in the MPS is reduced accordingly to the number of extracted features. Here, for any feature qubit $|s_n\rangle$, we characterize its entanglement using the entanglement entropy

$$S^{[n]} = -\text{Tr} \hat{\rho}^{[n]} \ln \hat{\rho}^{[n]}, \quad (6)$$

where $\hat{\rho}^{[n]} = \text{Tr}_{/s_n} |\Psi\rangle\langle\Psi|$, and $\text{Tr}_{/s_n}$ traces over all degrees of freedom except s_n . Under such an optimization scheme, we are able to represent and classify hand-written digits of “0” and “1” in the MNIST dataset [26] accurately using only three or five feature states $\{|\psi_i\rangle\}$, which we demonstrate via a photonic simulator below.

Experimental implementation.—As shown in Fig. 1b, we experimentally demonstrate two different classifier schemes (Scheme A and Scheme B) with exactly reverse processes. In either case, we embed core features of an image into the quantum feature space of three or five feature states $\{|\psi_i\rangle\}$, which corresponds to a three- or five-layer construction that involves their respective number of unitary gate operations. While these different constructions enable us to explore the impact of feature-

space dimension on the behavior of quantum classifier, the gate operations under a given scheme and construction are determined in the training process on a classical computer. In Fig. 1b, we show the qubit-efficient scheme [35] of a five-layer construction as an example, where arrows indicate the direction of flow for different schemes. For both schemes, we use two physical qubits, a classifier qubit and an operational qubit, to carry out the classification.

In Scheme A, we initialize the classifier and operational qubits into feature states $|\psi_1\rangle$ and $|\psi_2\rangle$, respectively. The other feature states are used as successive inputs for the optimized quantum circuit consisting of a series of single- and two-qubit gates U_i . We perform a projective measurement $\sigma_z = |0\rangle\langle 0| - |1\rangle\langle 1|$ on the output classifier qubit, yielding probabilities P_0 and P_1 . The image is recognized as “0” (“1”) for $P_0 > P_1$ ($P_1 > P_0$).

In Scheme B, we initialize the classifier and operational qubits into the two-qubit state $|00\rangle$ (or $|10\rangle$), and successively apply the optimized unitary gates U_i^\dagger (in the reverse order compared to that in Scheme A). A projective measurement $|\psi_i\rangle\langle\psi_i|$ is performed following the corresponding unitary operation U_i^\dagger . The last projective measurement $|\psi_1\rangle\langle\psi_1|$ on the classifier qubit yields the probability P'_0 (P'_1) for the initial state $|00\rangle$ (or $|10\rangle$). Since $P_0 = P'_0$ and $P_1 = P'_1$ (see Supplemental Materials), the image is recognized as “0” (“1”) for $P'_0 > P'_1$

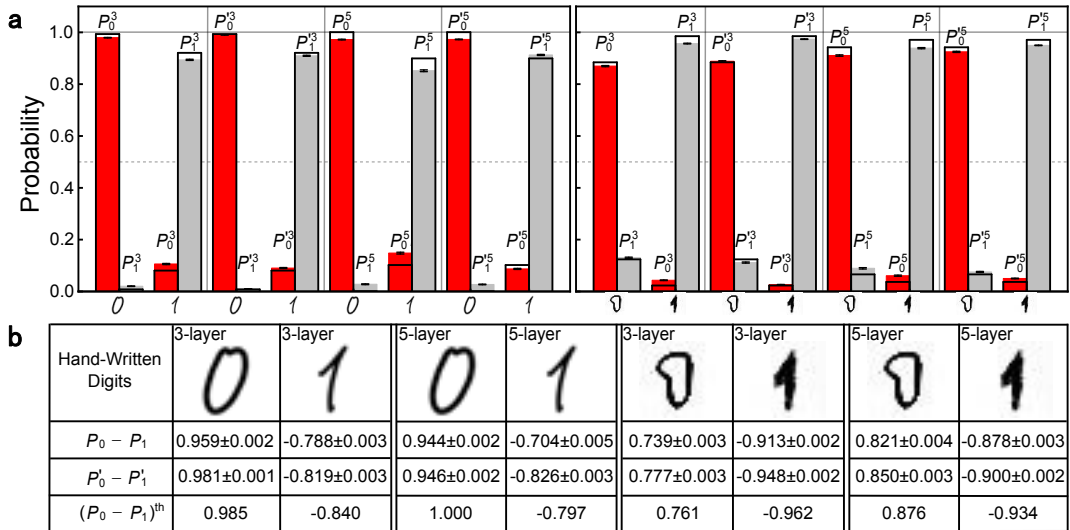


FIG. 5. **Classification of images outside the MNIST dataset.** **a** Measured probabilities of the output states of quantum classifiers (Scheme A and Scheme B). Colored bars: experimental results; hollow bars: theoretical predictions. Error bars indicate the statistical uncertainty, obtained by assuming Poissonian statistics. **b** Classification results.

($P'_1 > P'_0$).

Experimentally, as illustrated in Fig. 2 (taking the three-layer construction as an example), we encode the classifier qubit in the polarization states of the signal photons, i.e., $|H\rangle = |0\rangle$ and $|V\rangle = |1\rangle$. The operational qubit is encoded in the spatial modes of the photons, with $|u\rangle = |0\rangle$ and $|d\rangle = |1\rangle$ representing the upper and lower spatial modes, respectively. While the single-qubit gate U_1 is implemented using a half-wave plate (HWP), the two-qubit gates U_i ($i = 2, 3$) are implemented through cascaded interferometers, consisting of HWPs and beam displacers (BDs). In Scheme A, feature states $|\psi_i\rangle$ ($i = 2, 3$) are introduced via a controlled beam splitter (CBS), which consists of HWPs and BDs, with information of the feature states encoded in the setting angles of the HWPs.

Experimental results:—The gates are trained by 12665 hand-written digits of “0” and “1” in the training set of the MNIST dataset [26]. After the training process, U_i are fixed for subsequent image recognition. To assess the training process, we first use 2115 images in the testing set of the MNIST dataset as input. As illustrated in Fig. 3, under the three-layer construction, the classifier fails to recognize only 30 out of the 2115 images, including 10 images of “0” and 20 images of “1”. The success probability of classification is 0.9858. Under the five-layer construction, the classifier fails to recognize 19 images within the same testing set, including 4 images of “0” and 15 images of “1”. The success probability is 0.9910.

Figure 4 demonstrate in detail the results of several typical testing images as examples. For all chosen images, the experimental results suggest that the classifiers are well-trained, in the sense that their predictions have a high success rate, even if the probability differ-

ence $P_0 - P_1$ ($P'_0 - P'_1$) can be small for certain cases. Furthermore, some images that cannot be classified under the three-layer construction can be successfully classified under the five-layer construction, confirming the improvement in behavior of the quantum classifier with an increased feature-space dimension.

To estimate the deviation of the experimental results and theoretical predictions, we define a distance

$$d := \sqrt{\frac{(P_0 - P_0^{\text{th}})^2 + (P_1 - P_1^{\text{th}})^2}{2}}, \quad (7)$$

where $P_{0,1}$ and $P_{0,1}^{\text{th}}$ are the measured probabilities and theoretical probabilities, respectively. The distance varies between 0 and 1, with 0 indicating a perfect match. Of all eight distances for the images in Fig. 4, the largest is 0.039 ± 0.003 , which indicates that our experimental results are in excellent agreement with theoretical predictions.

To provide a quantitative estimate of the success rate of our quantum classifier, we perform numerical simulations by considering experimental imperfections, such as fluctuations in photon numbers, the inaccuracy of wave plates, and the dephasing due to the misalignment of BDs. We parameterize these experimentally imperfections using typical experimental parameters as well as the experimental data for the images in Fig. 4 (see Methods). We then perform Monte Carlo simulations of the experimental process for a numerical estimation of the success rate. For all 2115 images in our testing set, the estimated success rates are above 98% for all experiments.

Finally, in Fig. 5 we show the results of applying the trained classifier on two pairs of hand-written digits “0” and “1” that are not in the MNIST dataset. The first pair of digits are written in a standard way. The second pair is

written such that the profile of “0” resembles that of “1” in the first pair, and the profile of “1” is much shorter and fatter compared to its counterpart in the first pair. For both cases, our classifier correctly recognizes the images with high confidence (large $|P_0 - P_1|$), demonstrating the robustness and accuracy of the device.

Discussion.—We report the first experimental demonstration of quantum image classification of real-life, hand-written images. The experimental scheme adopts a TN-based machine learning algorithm, which benefits from the powerful interpretability of TNs, as well as our efficient entanglement-based optimization in the quantum feature space. The TN-based machine learning algorithm demonstrated here is general, and directly applicable to a wide range of physical platforms. In particular, with the rapid progress in quantum computers based on superconducting quantum circuits [32], it is hopeful that TN-based machine learning can be demonstrated for a larger feature space with more qubits, such that it can

find utilities in more complicated real-world tasks.

ACKNOWLEDGMENTS

This work has been supported by the Natural Science Foundation of China (Grant No. 11674056, No. 11674189, No. U1930402, and No. 11974331) and the startup fund from Beijing Computational Science Research Centre. KKW acknowledges support from the Project Funded by China Postdoctoral Science Foundation (Grant No. 2019M660016). WY acknowledges support from the National Key Research and Development Program of China (Grant Nos. 2016YFA0301700 and 2017YFA0304100). SJR is supported by Beijing Natural Science Foundation (Grant No. 1192005 and No. Z180013) and in part by the NSFC (Grant No. 11834014), and by the Academy for Multidisciplinary Studies, Capital Normal University.

Appendix A: Determine the gates U_i through TN representation

The tensors in the MPS satisfy the right-to-left orthogonal conditions as

$$\sum_{s_N a_{N-1}} A_{s_N, c a_{N-1}}^{[N]} A_{s_N, c' a_{N-1}}^{[N]} = \mathbb{1}_{cc'}, \quad (\text{A1})$$

$$\sum_{s_n a_{n-1}} A_{s_n, a_n a_{n-1}}^{[n]} A_{s_n, a'_n a_{n-1}}^{[n]} = \mathbb{1}_{a_n a'_n}, \quad (\text{A2})$$

$$\sum_{s_1} A_{s_1, a_1}^{[1]} A_{s_1, a'_1}^{[1]} = \mathbb{1}_{a_1 a'_1}, \quad (\text{A3})$$

where $\mathbb{1}$ denotes the identity and $n = 2, \dots, N-1$ in Eq. (A2). With these orthogonal conditions, the MPS represents a renormalization-group flow from the right to the label index located at the left end.

The orthogonal conditions allow us to encode the MPS into a quantum circuit that is executable on quantum platforms [35, 42]. To use only single- and two-qubit gates in the circuit, we set $N_c = \dim(c) = \dim(a_n) = 2$. Some matrix components of the gates are given directly by the tensors in the MPS as

$$\langle 0c | U_N | s_N a_{N-1} \rangle = A_{s_N, c a_{N-1}}^{[N]}, \quad (\text{A4})$$

$$\langle 0a_n | U_n | s_n a_{n-1} \rangle = A_{s_n, a_n a_{n-1}}^{[n]}, \quad (\text{A5})$$

$$\langle s_1 | U_1 | a_1 \rangle = A_{s_1, a_1}^{[1]}. \quad (\text{A6})$$

Other components are determined from the orthogonal conditions

$$\langle 0c | U_N U_N^\dagger | 1c' \rangle = 0 \quad (\text{A7})$$

$$\langle 0a_n | U_n U_n^\dagger | 1a'_n \rangle = 0, \quad (\text{A8})$$

and the orthonormal conditions

$$\langle 1c | U_N U_N^\dagger | 1c' \rangle = \mathbb{1}_{cc'}, \quad (\text{A9})$$

$$\langle 1a_n | U_n U_n^\dagger | 1a'_n \rangle = \mathbb{1}_{a_n a'_n}. \quad (\text{A10})$$

After getting the matrix elements of all gate operations, we numerically determine the parameters of the photonic interferometry network.

Feature extraction. Consider a square, gray-scale image consisting of N pixels, with the value of the pixel on the i th row and j th column characterized by $x_{i,j}$ ($0 \leq x_{i,j} \leq 1$). To lower the required number of features for image

classification, we transform the classical image data in the pixel space $\{x\}$ to the frequency space $\{y\}$ using a discrete cosine transformation

$$y_{p,q} = \frac{2}{H} \alpha(p-1) \alpha(q-1) \sum_{i=1}^H \sum_{j=1}^H x_{i,j} \cos \left[\frac{(2i-1)(p-1)\pi}{2H} \right] \cos \left[\frac{(2j-1)(q-1)\pi}{2H} \right]. \quad (\text{A11})$$

Here H is the height/width of the square image (in units of pixels), $p, q \in \{1, \dots, H\}$, and $0 \leq y_{p,q} \leq 1$. The factor $\alpha(p) = 1/\sqrt{2}$ for $p = 1$, and $\alpha(p) = 1$ otherwise. In our case, we have $H = 28$ for images in the MNIST dataset. The product state in Eq. (1) is therefore obtained by applying the feature map to the frequencies $\{y\}$.

To complete the feature extraction of the image, we retain a small number of feature qubits that have the largest entanglement entropy in the quantum feature space, according to Eq. (6). Such a feature extraction scheme enables us to represent and classify hand-written digits of “0” and “1” in the MNIST dataset with only three or five feature qubits, which is crucial for implementing the classifier on our photonic simulator. We note that since high-frequency components of the original image are mostly discarded in the cosine transformation, our scheme should also be robust to high-frequency noise in the hand-written image.

Appendix B: Gate-operation sequence in the two schemes

We use the three-layer construction as an example to introduce the gate-operation sequences in the experiment. Under the three-layer construction, we have three feature states $\{|\psi_1\rangle, |\psi_2\rangle, |\psi_3\rangle\}$, as well as three unitary operators $\{U_1, U_2, U_3\}$ that are fixed after the training process.

For Scheme A, we initialize the classifier and the operational qubits, respectively, in the feature states $|\psi_1\rangle$ and $|\psi_2\rangle$. The classifier qubit is then subject to the single-qubit operator U_1 , whose output is fed into the two-qubit operation U_2 together with the operational qubit. After projecting the operational qubit into the basis state $|0\rangle$, the classifier qubit is characterized by the density matrix

$$\rho_1 = \text{Tr}_{\text{op}} \left[U_2 \left(U_1 |\psi_1\rangle \langle \psi_1| U_1^\dagger \otimes |\psi_2\rangle \langle \psi_2| \right) U_2^\dagger (\mathbb{1} \otimes |0\rangle \langle 0|) \right]. \quad (\text{B1})$$

Here Tr_{op} is the trace over the two-dimensional Hilbert space of the operational qubit. The operational qubit is then prepared in the feature state $|\psi_3\rangle$, before the two-qubit operator U_3 is applied on both qubits. After projecting the operational qubit into the basis state $|0\rangle$ again, the classifier qubit is given by

$$\rho_2 = \text{Tr}_{\text{op}} \left[U_3 (\rho_1 \otimes |\psi_3\rangle \langle \psi_3|) U_3^\dagger (\mathbb{1} \otimes |0\rangle \langle 0|) \right]. \quad (\text{B2})$$

Finally, a projective measurement of σ_z is applied on the classifier qubit. The difference between the probabilities $P_0 = \text{Tr}[\rho_2 |0\rangle \langle 0|]$ and $P_1 = \text{Tr}[\rho_2 |1\rangle \langle 1|]$ indicates the result of the classification. Specifically, if $P_0 > P_1$ ($P_0 < P_1$), the image is recognized as “0” (“1”).

For Scheme B, we initialize the operational and the classifier qubits in a two-qubit state $|00\rangle$ ($|10\rangle$), and apply the two-qubit operation U_3^\dagger , followed by a projective measurement $|\psi_3\rangle \langle \psi_3|$ on the operational qubit. The classifier qubit is then characterized by

$$\rho_{1i} = \text{Tr}_{\text{op}} \left[U_3^\dagger (|i\rangle \langle i| \otimes |0\rangle \langle 0|) U_3 (\mathbb{1} \otimes |\psi_3\rangle \langle \psi_3|) \right], \quad (\text{B3})$$

where $i = 0, 1$ denotes the initial state of the classifier qubit. We then prepare the operational qubit in the state $|0\rangle$, and apply the two-qubit operator U_2^\dagger on both qubits. Then, after a projective measurement $|\psi_2\rangle \langle \psi_2|$ on the operational qubit, the classifier qubit is given by

$$\rho_{2i} = \text{Tr}_{\text{op}} \left[U_2^\dagger (\rho_{1i} \otimes |0\rangle \langle 0|) U_2 (\mathbb{1} \otimes |\psi_2\rangle \langle \psi_2|) \right]. \quad (\text{B4})$$

Finally, a single-qubit gate U_1^\dagger is applied to the classifier qubit, followed by a projective measurement $|\psi_1\rangle \langle \psi_1|$. The projective measurement yields the probabilities $P'_i = \text{Tr} \left[U_1^\dagger \rho_{2i} U_1 |\psi_1\rangle \langle \psi_1| \right] / N$, where $i = 0, 1$ and $N = \sum_{i=1,2} \text{Tr} \left[U_1^\dagger \rho_{2i} U_1 |\psi_1\rangle \langle \psi_1| \right]$. Similar to Scheme A, the difference $P'_0 - P'_1$ gives the result of classification. In fact, Scheme B is the reverse process of Scheme A, and we have $P_0 = P'_0$ and $P_1 = P'_1$ (see Supplemental Materials for a proof).

Appendix C: Experimental details

Experimentally, we create a pair of photons via spontaneous parametric down conversion, of which one serves as a trigger and the other serves as the signal [43]. The signal photon is then sent to the interferometry network. For both of our schemes, we encode the classifier qubit in the polarization of the signal photon, with $|H\rangle$ and $|V\rangle$ corresponding to the horizontally and vertically polarized photons, respectively. The operational qubit is encoded in the spatial modes of the signal photon, with $|u\rangle$ and $|d\rangle$ representing the upper and lower spatial modes.

For both schemes, the single-qubit gate U_1 is realized by a HWP on the polarization of photons. In Scheme A, to prepare for the input of the two-qubit gates U_i ($i = 2, 3$), the feature states, encoded in the spatial modes of photons as $\gamma|u\rangle + \eta|d\rangle$, are introduced by CBSs that expands the dimensions of the system: $\alpha|H\rangle + \beta|V\rangle \rightarrow (\alpha|H\rangle + \beta|V\rangle) \otimes (\gamma|u\rangle + \eta|d\rangle)$. A CBS is realized by three BDs and five HWPs. The first BD splits photons into different spatial modes depending on their polarizations. The following HWPs and BDs realize a controlled two-qubit gate on the polarizations and spatial modes of photons. Note that parameters of the unitary operators U_i are fixed during the training process, which are encoded through the angles of HWPs.

The two-qubit gate U_i is implemented by a cascaded interferometer. As an arbitrary 4×4 matrix, U_i can be decomposed using the cosine-sine decomposition method [44], where $U_2 = LSR$, with L , R and S controlled two-qubit gates. L and R are realized by inserting the HWPs in the corresponding spatial mode, in which spatial mode serves as the control qubit and the polarization is the target qubit. For S , the polarization is the control qubit and the spatial mode is the target qubit. Thus, it can be further decomposed into a SWAP gate and a controlled gate, in which spatial mode is the control qubit and the polarization is the target one. These are realized by four BDs and several HWPs. In between each two-qubit gates, we use a 1m long single-mode fiber to connect cascaded interferometers and act as a spatial filter.

Appendix D: Estimation of the success rate of the quantum classifier

The differences between the experimental data and theoretical predictions are caused by several factors, including fluctuations in photon numbers, the inaccuracy of wave plates, and the dephasing due to the misalignment of the BDs. To provide a quantitative estimate of the success rate of our quantum classifier, we perform numerical simulations by taking experimental imperfections into account.

First, the imperfection caused by photon-number fluctuations increases with decreasing photon counts. In our experiment, the total photon count for each image classification is larger than 1×10^4 . Therefore, we adopt a total photon count $N = 1 \times 10^4$ for our estimation, while assuming a Poissonian distribution in the photon statistics. Second, parameters characterizing the inaccuracy of wave plates and the dephasing are estimated using experimental data in Fig. 4. Specifically, for each wave plate, we assume an uncertainty in the setting angle $\theta + \delta\theta$, where $\delta\theta$ is randomly chosen from the interval $[-1.588^\circ, 1.588^\circ]$ ($[-1.180^\circ, 1.180^\circ]$) under the three-layer (five-layer) construction. The range of these intervals are determined through Monte Carlo simulations, to fit the deviations of experimental data from their theoretical predictions for the eight images in Fig. 4. On the other hand, the dephasing due to the misalignment of BDs affects the experimental results through a noisy channel $\varepsilon(\rho) = \eta\rho + (1 - \eta)\sigma_z\rho\sigma_z$ characterized by a dephasing rate η [45], where ρ ($\varepsilon(\rho)$) is the density matrix of the input (output) state of the noise channel, and σ_z is a Pauli matrix. By numerically minimizing the difference between the numerical results and the corresponding experiment data, we estimate η to be 0.9977 (0.9926) for three-layer (five-layer) construction.

With these, we perform Monte Carlo simulations of our experiments on all 2115 images in the testing set, from which a success rate is estimated. We then repeat the process for 100 times and keep the lowest success rate as our final estimation. The estimated success rates are the following: 0.9825 (Scheme A with three-layer construction); 0.9820 (Scheme B with three-layer construction); 0.9877 (Scheme A with five-layer construction); 0.9877 (Scheme B with five-layer construction). Thus for all experiments, the success rates are above 98%.

Appendix E: Equivalence between two schemes of quantum classifier

The experimental setup for Scheme B is illustrated in Fig. 6, which is essentially the reverse process of Scheme A shown in Fig. 2 of the main text. Under Scheme B with the initial state $|00\rangle$, the probability P'_0 given by the last projective measurement can be written as (not normalized)

$$P'_0 = \text{Tr} \left[U_1^\dagger \rho_{20} U_1 |\psi_1\rangle \langle \psi_1| \right] = \text{Tr} \left[\text{Tr}_{\text{op}} \left(U_2^\dagger (\rho_{10} \otimes |0\rangle \langle 0|) U_2 (\mathbf{1} \otimes |\psi_2\rangle \langle \psi_2|) \right) U_1 |\psi_1\rangle \langle \psi_1| U_1^\dagger \right] = \text{Tr} [(\rho_{10} \otimes |0\rangle \langle 0|) \tilde{\rho}],$$

where $\tilde{\rho} = U_2 \left(U_1 |\psi_1\rangle \langle \psi_1| U_1^\dagger \otimes |\psi_2\rangle \langle \psi_2| \right) U_2^\dagger$. Hence, P'_0 can be regarded as the joint probability of two local, projective measurements on $\tilde{\rho}$, with the outcome of the classifier qubit given by ρ_{10} and that of the operational qubit given by $|0\rangle$. The probability can be re-arranged as

$$\begin{aligned} P'_0 &= \text{Tr} [\text{Tr}_{\text{op}} (\tilde{\rho} (\mathbf{1} \otimes |0\rangle \langle 0|)) \rho_{10}] = \text{Tr} \left[\rho_1 \text{Tr}_{\text{op}} \left(U_3^\dagger |00\rangle \langle 00| U_3 (\mathbf{1} \otimes |\psi_3\rangle \langle \psi_3|) \right) \right] \\ &= \text{Tr} \left[U_3^\dagger |00\rangle \langle 00| U_3 (\rho_1 \otimes |\psi_3\rangle \langle \psi_3|) \right] = \text{Tr} \left[|00\rangle \langle 00| U_3 (\rho_1 \otimes |\psi_3\rangle \langle \psi_3|) U_3^\dagger \right]. \end{aligned}$$

On the other hand, for Scheme A, the probability of the projective measurement σ_z on the output classifier qubit is (not normalized)

$$\begin{aligned} P_0 &= \text{Tr} [\rho_2 |0\rangle \langle 0|] = \text{Tr} \left[\text{Tr}_{\text{op}} \left(U_3 (\rho_1 \otimes |\psi_3\rangle \langle \psi_3|) U_3^\dagger (\mathbf{1} \otimes |0\rangle \langle 0|) \right) |0\rangle \langle 0| \right] \\ &= \text{Tr} \left[U_3 (\rho_1 \otimes |\psi_3\rangle \langle \psi_3|) U_3^\dagger |00\rangle \langle 00| \right] = P'_0. \end{aligned}$$

Similarly, as $P_0 + P_1 = P'_0 + P'_1 = 1$, we have $P_1 = P'_1$. Thus, we prove the equivalence of the two schemes.

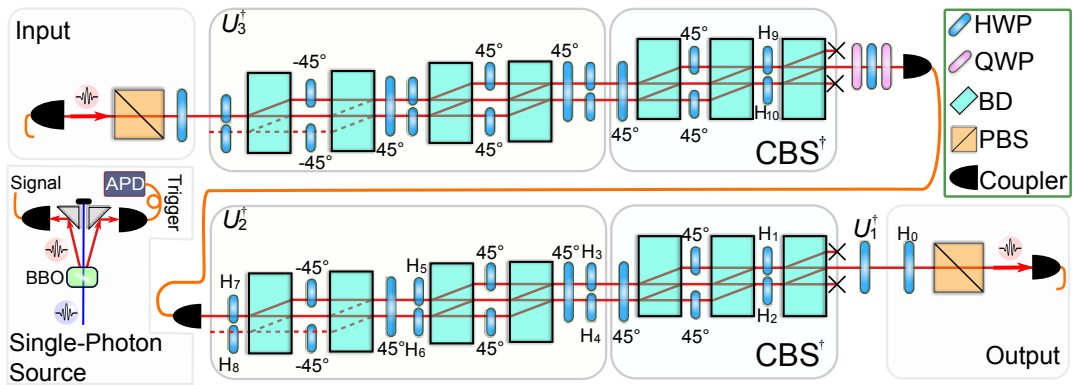


FIG. 6. **Experimental demonstration of quantum classifier under Scheme B (three-layer construction).** The classifier and operational qubits are initialized in $|H\rangle \otimes |u\rangle$ or $|V\rangle \otimes |u\rangle$ via a PBS and a HWP. After each gate operation U_i^\dagger ($i = 1, 2, 3$), a projective measurement $|\psi_i\rangle \langle \psi_i|$ is performed on the operational qubit via a CBS. This is the reverse process of the setup in Fig. 1 of the main text.

- [1] Biamonte, J. *et al.* Quantum machine learning. *Nature* **549**, 195 (2017).
- [2] Dunjko, V. & Briegel, H. J. Machine learning & artificial intelligence in the quantum domain: a review of recent progress. *Rep. Prog. Phys.* **81**, 074001 (2018).
- [3] Havlíček, V. *et al.* Supervised learning with quantum-enhanced feature spaces. *Nature* **567**, 209 (2019).
- [4] Cong, I., Choi, S. & Lukin, M. D. Quantum convolutional neural networks. *Nature Phys.* **15**, 1273 (2019).
- [5] Schuld, M. & Killoran, N. Quantum machine learning in feature Hilbert spaces. *Phys. Rev. Lett.* **122**, 040504 (2019).
- [6] Verstraete, F., Murg, V. & Cirac, J. I. Matrix product states, projected entangled pair states, and variational renormalization group methods for quantum spin systems. *Adv. Phys.* **57**, 143 (2008).
- [7] Cirac, J. I. & Verstraete, F. Renormalization and tensor product states in spin chains and lattices. *J. Phys. A: Math. Theor.* **42**, 504004 (2009).
- [8] Haegeman, J. & Verstraete, F. Diagonalizing transfer matrices and matrix product operators: a medley of exact and computational methods. *Annu. Rev. Condens. Matter Phys.* **8**, 355 (2017).
- [9] Ran, S.-J. *et al.* *Tensor Network Contractions: Methods and Applications to Quantum Many-Body System*. Lecture Notes in Physics Vol. 964 (Springer, Cham, Switzerland, 2020).
- [10] Sun, Z.-Z., Peng, C., Liu, D., Ran, S.-J., & Su, G. Generative tensor network classification model for supervised machine learning. *Phys. Rev. B* **101**, 075135 (2020).
- [11] Reberstrost, P., Mohseni, M. & Lloyd, S. Quantum support vector machine for big data classification. *Phys. Rev. Lett.* **113**, 130503 (2014).
- [12] Anguita, D., Ridella, S., Riviaccio, F. & Zunino, R.

- Quantum optimization for training support vector machines. *Neural Netw.* **16**, 763 (2003).
- [13] Li, Z., Liu, X., Xu, N. & Du, J. Experimental realization of a quantum support vector machine. *Phys. Rev. Lett.* **114**, 140504 (2015).
- [14] You, Y.-Z., Yang, Z. & Qi, X.-L. Machine learning spatial geometry from entanglement features. *Phys. Rev. B* **97**, 045153 (2018).
- [15] Levine, Y., Sharir, O., Cohen, N. & Shashua, A. Quantum entanglement in deep learning architectures. *Phys. Rev. Lett.* **122**, 065301 (2019).
- [16] Deng, D.-L., Li, X. & Sarma, S. D. Quantum entanglement in neural network states. *Phys. Rev. X* **7**, 021021 (2017).
- [17] Stoudenmire, E. & Schwab, D. J. *Supervised learning with tensor networks*. Advances in Neural Information Processing Systems 29 (ed. by Lee, D. D. *et al.*) 4799–4807 (Curran Associates, Red Hook, 2016).
- [18] Liu, D. *et al.* Machine learning by unitary tensor network of hierarchical tree structure. *New J. Phys.* **21**, 073059 (2019).
- [19] Han, Z.-Y., Wang, J., Fan, H., Wang, L. & Zhang, P. Unsupervised generative modeling using matrix product states. *Phys. Rev. X* **8**, 031012 (2018).
- [20] Guo, C., Jie, Z., Lu, W. & Poletti, D. Matrix product operators for sequence-to-sequence learning. *Phys. Rev. E* **98**, 042114 (2018).
- [21] Stoudenmire, E. M. Learning relevant features of data with multi-scale tensor networks. *Quantum Sci. Technol.* **3**, 034003 (2018).
- [22] Cheng, S., Wang, L., Xiang, T. & Zhang, P. Tree tensor networks for generative modeling. *Phys. Rev. B* **99**, 155131 (2019).
- [23] Glasser, I., Sweke, R., Pancotti, N., Eisert, J. & Cirac, I. *Expressive power of tensor-network factorizations for probabilistic modeling*. Advances in Neural Information Processing Systems 32 1496–1508 (Curran Associates, Red Hook, 2019).
- [24] Efthymiou, S., Hidary, J. & Leichenauer, S. Tensor Network for machine learning. Preprint at <https://arxiv.org/abs/1906.06329> (2019).
- [25] Liu, Y., Zhang, X., Lewenstein, M. & Ran, S.-J. Entanglement-guided architectures of machine learning by quantum tensor network. Preprint at <https://arxiv.org/abs/1803.09111> (2018).
- [26] Deng, L. The MNIST database of handwritten digit images for machine learning research [best of the web]. *IEEE Signal Proc. Mag.* **29**, 141-142 (2012).
- [27] Pepper, A., Tischler, N. & Pryde, G. J. Experimental realization of a quantum autoencoder: the compression of qutrits via machine learning. *Phys. Rev. Lett.* **122**, 060501 (2019).
- [28] Lau, H.-K., Pooser, R., Siopsis, G. & Weedbrook, C. Quantum machine learning over infinite dimensions. *Phys. Rev. Lett.* **118**, 080501 (2017).
- [29] Gao, X., Zhang, Z.-Y. & Duan, L.-M. A quantum machine learning algorithm based on generative models. *Sci. Adv.* **4**, eaat9004 (2018).
- [30] Cai, X.-D. *et al.* Entanglement-based machine learning on a quantum computer. *Phys. Rev. Lett.* **114**, 110504 (2015).
- [31] Zhang, D.-B., Zhu, S.-L. & Wang, Z. D. Protocol for implementing quantum nonparametric learning with trapped ions. *Phys. Rev. Lett.* **124**, 010506 (2020).
- [32] Arute, F. *et al.* Quantum supremacy using a programmable superconducting processor. *Nature* **574**, 505 (2019).
- [33] Zhu, D. *et al.* Training of quantum circuits on a hybrid quantum computer. *Sci. Adv.* **5**, eaaw9918 (2019).
- [34] Bartkiewicz, K. *et al.* Experimental kernel-based quantum machine learning in finite feature space. Preprint at <https://arxiv.org/abs/1906.04137> (2019).
- [35] Huggins, W., Patil, P., Mitchell, B., Whaley, K. B. & Stoudenmire, E. M. Towards quantum machine learning with tensor networks. *Quantum Sci. Technol.* **4**, 024001 (2019).
- [36] Gao, J. *et al.* Experimental machine learning of quantum states. *Phys. Rev. Lett.* **120**, 240501 (2018).
- [37] Hu, L. *et al.* Quantum generative adversarial learning in a superconducting quantum circuit. *Sci. Adv.* **5**, eaav2761 (2019).
- [38] Hentschel, A. & Sanders, B. C. Machine learning for precise quantum measurement. *Phys. Rev. Lett.* **104**, 063603 (2010).
- [39] Lian, W. *et al.* Machine learning topological phases with a solid-state quantum simulator. *Phys. Rev. Lett.* **122**, 210503 (2019).
- [40] Pérez-García, D., Verstraete, F., Wolf, M. M. & Cirac, J. I. Matrix Product State Representations. *Quantum Inf. Comput.* **7**, 401 (2007).
- [41] PBishop, C. M. *Pattern recognition and machine learning*. Information science and statistics (Springer, New York, 2006).
- [42] Schön, C., Solano, E., Verstraete, F., Cirac, J. I. & Wolf, M. M. Sequential generation of entangled multi-qubit states. *Phys. Rev. Lett.* **95**, 110503 (2005).
- [43] Xiao, L. *et al.* Observation of topological edge states in parity-time-symmetric quantum walks. *Nat. Phys.* **13**, 1117-1123 (2017).
- [44] Izaac, J. A. *et al.* Centrality measure based on continuous-time quantum walks and experimental realization. *Phys. Rev. A* **95**, 032318 (2017).
- [45] Wang, K. K. *et al.* Entanglement-enhanced quantum metrology in a noisy environment. *Phys. Rev. A* **97**, 042112 (2019).